Understanding the mechanism of capacity increase during early cycling of commercial NMC/graphite lithium-ion batteries

Guo, Jia; Li, Yaqi; Pedersen, Kjeld; Gurevich, Leonid; Stroe, Daniel-Ioan

Published in:
Journal of Energy Chemistry

DOI (link to publication from Publisher):
10.1016/j.jechem.2022.07.005

Publication date:
2022

Document Version
Publisher's PDF, also known as Version of record

Journal of Energy Chemistry 74 (2022) 34–44

Contents lists available at ScienceDirect

Journal of Energy Chemistry

journal homepage: www.elsevier.com/locate/jechem

http://www.journals.elsevier.com/journal-of-energy-chemistry/

Research article

Understanding the mechanism of capacity increase during early cycling of commercial NMC/graphite lithium-ion batteries

Jia Guo [a,b], Yaqi Li [a,b,*], Jinhao Meng [c], Kjeld Pedersen [b], Leonid Gurevich [b], Daniel-Ioan Stroe [a]

[a] AAU Energy, Aalborg University, Aalborg 9220, Denmark
[b] Department of Materials and Production, Aalborg University, Aalborg 9220, Denmark
[c] College of Electrical Engineering, Sichuan University, Chengdu 610065, Sichuan, China

ARTICLE INFO

Article history:
Received 23 May 2022
Revised 1 July 2022
Accepted 6 July 2022
Available online 12 July 2022

Keywords:
Capacity increasing
Lithium-ion battery
Full cell
Coin cell
Graphite anode

ABSTRACT

A capacity increase is often observed in the early stage of Li-ion battery cycling. This study explores the phenomena involved in the capacity increase from the full cell, electrodes, and materials perspective through a combination of non-destructive diagnostic methods in a full cell and post-mortem analysis in a coin cell. The results show an increase of 1% initial capacity for the battery aged at 100% depth of discharge (DOD) and 45 °C. Furthermore, large DODs or high temperatures accelerate the capacity increase. From the incremental capacity and differential voltage (IC-DV) analysis, we concluded that the increased capacity in a full cell originates from the graphite anode. Furthermore, graphite/Li coin cells show an increased capacity for larger DODs and a decreased capacity for lower DODs, thus in agreement with the full cell results. Post-mortem analysis results show that a larger DOD enlarges the graphite d-space and separates the graphite layer structure, facilitating the Li^+ diffusion, hence increasing the battery capacity.

1. Introduction

Lithium-ion (Li-ion) batteries have been widely used in electric vehicles (EVs) due to their high energy density, low self-discharge, and long lifetimes [1]. However, the inevitable degradation under charge/discharge cycle has significant consequences on safety and reliability of the battery system [2,3]. The aging behavior of batteries during the initial charge/discharge cycles is particularly critical for state-of-health analysis, lifetime prediction, and holds keys to the development of high-performance batteries [4]. A gradual capacity increase is one of the most anomalous behaviors in the early stages of battery cycling, which results in an increase in stored energy. This behavior may lead to unstable operation of a battery system or even cause accidents.

Some researchers used data-driving approaches to predict the battery cycling life and consider the capacity increases in their algorithms [5–8]. These approaches usually require extensive battery testing and large data sets. If the capacity increase can be understood from the perspective of underlying physical mechanisms perspective, the effect can be eliminated by improving cells' manufacturing process or by optimizing the charging and discharging profiles. Up to now, the mechanism responsible for the battery capacity increase or recovery during initial charge/discharge stages has been rarely studied.

Several previous studies, summarized in Table 1, have reported an increase in battery capacity during cycling aging; however, the understanding of the underlying mechanisms is limited. Gyenes et al. [9] proposed the so-called "overhang" mechanism to explain the increasing in capacity during aging. They have found that Li-ions are inserted into the overhang region of graphite anode during the high state of charge in initial cycles, followed by diffusion of Li-ions from the overhang regions in the subsequent cycling, hence causing a slight capacity excess. Nevertheless, it is still difficult to explain the continuous capacity increase over hundreds of cycles due to a limited amount of lithium ions deposited in overhangs. Lewerenz et al. [10] have extended this approach with the concept of the so-called "passive electrode", where the anode potential is affected by the potential difference between the active and the passive regions of the anode, which results in a low potential of the anode and a capacity rise of the full cell. However, these mechanisms cannot explain the variety of situations in which the capacity increased is observed. In [5], Severson et al. found a trend of capacity increase during the initial cycles for all the 124 aged cells. They explained this behavior by Dubarry's description, i.e., the loss of negative electrode material leads to a high potential difference in the cell [11]. Dubar-

* Corresponding author.
E-mail address: yaqili@mp.aau.dk (Y. Li).

https://doi.org/10.1016/j.jechem.2022.07.005

Table 1
An overview of the publications related to capacity increasing of Li-ion battery in cycling.

References	Electrodes	Battery type	Relative capacity increase/cycles	Mechanism suggested
Gyenes et al. [9]	NMC/graphite	Pouch cell	1%	Diffusion of Li ions from the overhang region of graphite anode.
Lewerenz et al. [10]	LFP/graphite	18650	0.4%–1.7%/200	Diffusion of Li ions from passive electrode areas.
Severson et al. [5]	LFP/graphite	A123 18650	0.2%/100	Loss of negative material change the potentials.
Dubarry et al. [11]	LFP/graphite	Coin cell	1%	Loss of negative electrode.
Kobayashi et al. [12]	LFP/graphite	Large-scale cells 100 Wh	20%/recovery cycling	Non uniform Li-ion distribution is formed under shallow cycling and leads to capacity loss. It can be restored.

ry's experiment is performed by simulating the loss of the negative electrode material, resulting in a rise of the voltage plateau of the full cell, and subsequently an increased capacity. Kobayashi et al. [12] aged the battery with a shallow depth-of-discharge (DOD) (40%–60%) for 250 days, and then trained it at 100% DOD. Surprisingly, the capacity lost during the shallow cycling, could be, to a large extent gradually recovered during the full cycles. The authors attributed it to a non-uniform distribution of Li-ions created during shallow cycling.

Overall, the experimental evidence points to the fact that the capacity increase is related to the extent of DOD. However, the mechanisms related to this behavior has not been fully explained yet.

The analysis in the above studies has been mainly focused on non-destructive methods such as electrochemistry simulation, characteristics of charging-discharging curves, and in-situ pulse test (e.g., electrochemical impedance spectroscopy (EIS)). These powerful techniques have been widely used in previous studies and carried out at full-cell level; however, those techniques are less effective at the electrode and/or material level.

Ex-situ techniques such as X-ray diffraction (XRD) and field emission scanning electron microscope (FESEM) can often provide in-depth analysis of the material and electrode degradation, revealing the internal aging mechanisms of the battery. Nevertheless, for this purpose, the cells have to be disassembled.

The framework reported in the present study combines both in-situ and ex-situ approaches to analyze the capacity-increasing mechanism on the full-cell, electrode, and material levels, ensuring that the full-cells under test are not destructed. Specifically: (1) the 18650 full cells are aged at different DODs and temperature to study the effect of those factors on capacity increase; (2) fresh positive electrode/Li-metal (NMC/Li), fresh positive electrode/fresh negative electrode (NMC/graphite), and fresh negative electrode/Li-metal (graphite/Li) are assembled in coin cells to analyze the degradation indicators from the electrochemical characteristic curves (IC-DV); (3) according to the degradation indicators in (2), the IC-DV curves from full cells are studied, and the aging mechanism in full cell level is analyzed by EIS; (4) according to the inference results from (3), the influence in capacity increasing is further studied at the coin cell level. Using this framework, the mechanism of capacity increase is thoroughly explained and discussed.

The structure of the paper is as follows: Section 2 describes the full cell aging experiment and presents details about coin cells fabrication and testing. Section 3 analyzes the data from full cell aging and deduces the targeted aging mechanism. Section 4 presents an in-depth analysis of the aging mechanism at both electrode and materials levels. Section 5 is a summary of our main conclusion.

2. Experimental

2.1. Full cell testing

Full cell testing was carried out on commercially available 18650 full cells, manufactured by Haidi company, with a capacity of 2.2 Ah and a nominal voltage of 3.7 V; $LiNi_{0.5}Co_{0.2}Mn_{0.3}O_2$ and synthetic graphite were used as cathode and anode materials, respectively. Seven cells were tested using a Digatron battery test station in four cycling cases, as summarized in Table 2. Two cells were tested for every test case, except for case 1, where one battery was tested. Thus, data from seven battery cells were collected. The test program is shown in Fig. S1.

Aging test: The cycling aging tests were performed based on the following procedure. Initially, the cells were charged to 4.2 V using a constant current-constant voltage (CC-CV) profile with a 0.5 C constant current. The cells were considered fully charged when the current decreased to 0.11 A. In the next step, the cells were discharged to certain SOC values, as summarized in Table 2, using a synthetic current profile with an average current of 0.19 C. The same synthetic current profile was used for all the four cases.

Reference performance test (RPT): To analyze and quantify the effect from the operating DODs and temperatures, RPTs at 25 °C were performed, after every 100 equivalent full cycles (EFCs). To measure the capacity, the cells were charged to 4.2 V using a CC-CV profile with a 0.5 C current; the cells were considered fully charged when the cut-off current reached a value of 0.11 A. After a one hour pause, the cells were discharged to 2.75 V under 0.5 C constant current. In addition, the EIS spectra of the cells were measured, using a Digatron Firing Circuits EIS analyzer, in the frequency range of 6.5 kHz to 10 mHz, considering high, medium, and low frequency points; the obtained EIS spectra were fitted with an appropriate equivalent circuit model using the ZsimDemo software (Ametek company), as presented in Section 3.3.

2.2. Coin cell assembly and testing

NMC positive electrodes and graphite negative electrodes were also provided by Haidi company, which are from the same batch as the electrodes used in the 18650 full cells. It is also feasible to obtain the electrodes from disassembling fresh 18650 full cells, so readers can refer to it if fresh electrodes cannot be obtained from the manufacturer. Both positive electrodes and negative elec-

Table 2
The test matrix for 18650 full cell aging.

	45% DOD	75% DOD	100% DOD
35 °C	Case 1	–	Case 2
45 °C	–	Case 3	Case 4

trodes were cut into 14 mm-diameter-discs, which were paired with 15 mm-diameter-lithium metal discs and assembled into 2016-coin cell cases. The electrolyte was 1 M LiF_6 in dimethyl carbonate (DMC)/diethyl carbonate (DEC) mixed in 1:1 ration, and the amount is 5 drops with a 1 mL pipette in each coin cell.

Coin cell test for degradation indicators: NMC/Li, NMC/graphite and graphite/Li were assembled as coin cells as described in the previous section. NMC/Li and NMC/graphite coin cell were charged with 0.1 C-rate (1 C = 150 mAh g^{-1}) to 4.2 V, then charged under constant voltage of 4.2 V until the current reduced to 0.01 mA; then, the cells were discharged to 2.75 V by 0.1 C constant current. The graphite/Li coin cells were charged and discharged between 1.5 and 0.001 V by a constant current of 0.4 mA which corresponds to a 0.1 C current (i.e., 0.15 mA) in the test of the NMC/Li and NMC/graphite coin cells.

Coin cell test for evaluating the graphite electrode: Graphite/Li coin cell were repeatedly charged and discharged by a constant current of 0.8 mA which is the same as 0.2 C current in the test of NMC/Li and NMC/graphite cells. The voltage ranges were set to 1.0–0.001 and 0.2–0.001 V, which correspond well with the graphite available capacity in the full cell with 100% DOD and 45% DOD. XRD (Panalytical company) was performed to measure the graphite anode structure at 45 kV with a scanning speed of 2°/min. The FESEM (Zeiss 1540 XB) was used to observe the graphite morphology at 20 keV.

3. Capacity increase in full cell

3.1. Capacity increase

The initial RPT tests revealed an abnormal capacity increase in some cells during the first 200–300 EFCs under the combined influence of DOD and temperature. Fig. 1 shows the state of health (SOH) evolution for full cells during the first 400 EFCs. After initial 200–300 EFCs, all the cells eventually showed an expected decline in capacity. In Fig. 1(a), we present the capacity evolution of the cells cycled under 45% DOD and 100% DOD at 35 °C. The cells aged at 100% DOD showed a slight increase in capacity in the first 100 EFCs, then the capacity started to decrease in later stages of the aging test. The cells aged at 45% DOD exhibit a decrease trend in capacity in initial 200 EFCs. A similar capacity increase trend was also observed for the cells aged at 45 °C, as shown in Fig. 1(b). In the first 200 EFCs, both the cases of 75% DOD and 100% DOD show capacity increase. For the 100% DOD aged cells, a 1% capacity increase is observed in the first 200 EFCs, after which a faster (than for cells aged at 75% DOD) capacity fade occurs. Regarding the influence of temperature for the cells aged at 100% DOD, the capacity increase by 1% at 45 °C, which is more obvious comparing with the 0.3% increase at 35 °C.

To summarize, for the tested battery cells, an increase in capacity, which appears in early aging stages, is more obvious for larger DODs (such as 100% DOD and 75% DOD). Furthermore, the temperature exacerbates this effect for 100% DOD cycling.

3.2. Analysis of degradation indicators

To further study the capacity increase in 18650 cells at electrodes level, a number of advanced techniques have been used in literature to identify and quantify the electrochemical aging behavior in Li-ion batteries [13], such as incremental capacity and differential voltage (IC-DV) and EIS. These techniques use characteristic peaks or shape of the test curves as indicators to recognize battery aging.

3.2.1. Incremental capacity and differential voltage (IC-DV)

An IC curve is obtained by differentiating the battery capacity with respect to the voltage change, using Eq. (1), where Q_t and V_t correspond to the capacity and voltage at the time t [14,15]. The obtained IC plot shows the capacity contribution from certain voltage plateaus of batteries, and can be quantified by peak height, position, and area.

$$IC = \frac{dQ}{dV} = \frac{\Delta Q}{\Delta V} = \frac{Q_{t+1} - Q_t}{V_{t+1} - V_t} \quad (1)$$

Similar to an IC curve, a DV curve is defined as the derivative of voltage with respect to the charge or discharge capacity, using Eq. (2), which reflects a change in voltage with the capacity evolution [16]

$$DV = \frac{dV}{dQ} = \frac{\Delta V}{\Delta Q} = \frac{V_{t+1} - V_t}{Q_{t+1} - Q_t} \quad (2)$$

However, for IC and DV curves, the relationship between the indicators (change and shift in peaks) and the degradation behavior varies according to the type of electrode materials and the electrode parameters in a full cell. It is necessary to clarify the relation between the IC-DV indicators and the corresponding performance of the electrodes in a certain battery. Generally, electrochemical curve simulation is used to analyze the degradation indicators. However, it requires a detailed knowledge of over one hundred parameters in a full cell [17], which is difficult to collect. A slight error in parameters could lead to wrong simulation results and misunderstanding of the degradation indicators. Here, we propose

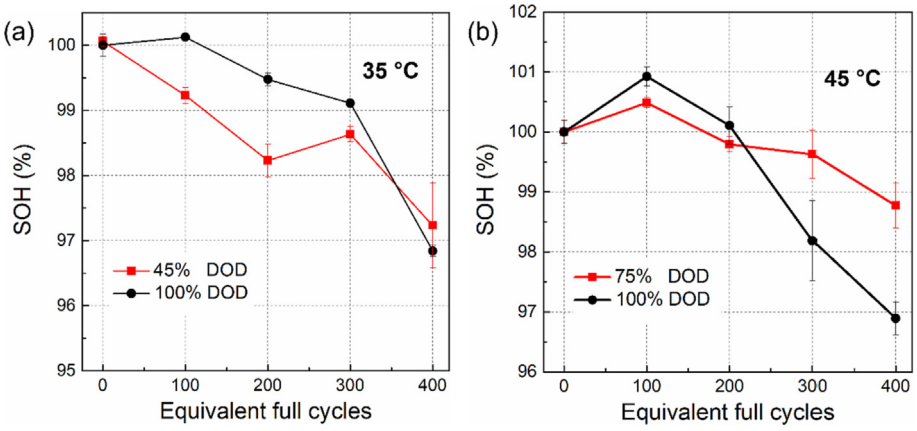

Fig. 1. Capacity fade in full cells during cycle aging at (a) 45% DOD and 100% DOD, at 35 °C, (b) 75% DOD and 100% DOD at 45 °C. The RPT test were carried out in the voltage range of 2.75–4.2 V with 0.5 C-rate (1.1 A) at 25 °C; error bars represent the standard deviation between two cells in each case.

to use coin cell batteries to compare the difference in IC and DV curves between half-cells (NMC/Li and Graphite/Li) and full coin cells (NMC/Graphite). Afterwards the degradation indicators will be clearly analyzed at electrode level.

Fig. 2(a) shows the charging-discharging (*Q*-*V*) curves of NMC/Li, NMC/Graphite and Graphite/Li coin cells, respectively. Overall, the shapes of NMC/Li and NMC/Graphite curves are similar and exhibit the typical high voltage plateau for NMC positive electrode. There are several distinctions between the two curves, where the graphite voltage governs the gap between the curves of NMC/Li and NMC/Graphite by transforming between pure graphite and LiC_6. That is reflected in a higher voltage plateau of NMC/Li and a rapid voltage rise in early stage of charging curve for NMC/Graphite. Based on the *Q*-*V* curves in Fig. 2(a), the corresponding DV curves were obtained and are shown in Fig. 2(b). Peaks in DV curves mark transitions between the two adjacent voltage plateaus in Fig. 2(a). Therefore, a shift in the peaks positions corresponds to a change in the duration time of voltage plateaus, which, in turn, is related to the amount of active material in the electrodes. Consequently, the left shift of DV peaks means that the amount of Li-intercalatable active materials in the respective electrode is reduced. Conversely, a shift of DV peaks to the right means an increase in the amount Li-intercalatable active materials. The NMC/Graphite DV curves show three evident peaks "I", "II", and "III", corresponding well to the peaks in DV curve for the Graphite/Li cell. In contrast, there is no obvious peak in the DV curve for NMC/Li, which means that the potential on the positive electrode changes smoothly during charging. Hence, I, II, and III peaks visible in Fig. 2(b) are determined by the graphite anode changing the state from C to LiC_6.

The peaks in the IC curves represent phase transitions during electrochemical reactions, which related to the plateaus in voltage profiles and valleys in DV curves, respectively. The peaks represent the battery capacity increase in certain voltage intervals. Compared with DV curves, IC curves present cell degradation indicators as a function of voltage, which provides a better reference to the state of a battery as compared to the capacity dependence [11]. As shown in Fig. 2(c), the graphite anode has three pairs of oxidation/reduction peaks, which are the main reason for the gap between the IC curves corresponding to the NMC/Li and NMC/Graphite, as illustrated in Fig. 2(d). Regarding the NMC/Li cell, the IC curve shows only a pair of main oxidation/reduction peaks, which corresponds well with the only one DV valley in Fig. 2(b). The NMC/Graphite shows an extra pair of peaks V and V́, attributed to the graphite anode. Therefore, the intensity of the V peak represents the capacity of the graphite anode in a certain voltage plateau, which also indicates the amount of available graphite in the negative electrode.

3.2.2. Electrochemical impedance spectroscopy (EIS)

The impedance spectrum of a typical Li-ion cell is shown in Fig. 3. Although the figure is schematic, it was drawn based on the real 18650 full cell experiments. The impedance is composed of two partially overlapped semicircles from high frequency to middle frequency, and a straight slopping line at the low frequency end. The R_{ohm} represents the bulk resistance, which is related to the electric conductivity of electrolyte, separator, connector, and connection cable [18]. R_{sei} is the resistance caused by the solid-state interface film on the electrode surfaces. Its value corresponds to the diameter of the fitted semicircle at a relative high frequency region (about 6400–50 Hz). R_{ct} represents the charge-transfer resistance, corresponding to the diameter of the fitted semicircle at the medium frequency region (about 50–0.2 Hz), and the straight line in the low frequency region mainly corresponds to Li-ion diffusion resistance due to the concentration polarization [19]. The measured EIS data can be simulated by an equivalent circuit, like shown in the insert in Fig. 3(a), using ZsimDemo 3.30 software.

Furthermore, the Li^+ diffusion coefficient (D_{Li}^+) in the solid electrode can be calculated using Eq. (3), where the Warburg factor (σ) can be calculated by Eqs. (4) and (5) [20,21]

$$D_{Li^+} = \frac{R^2T^2}{2A^2n^2F^2C^2\sigma^2} \quad (3)$$

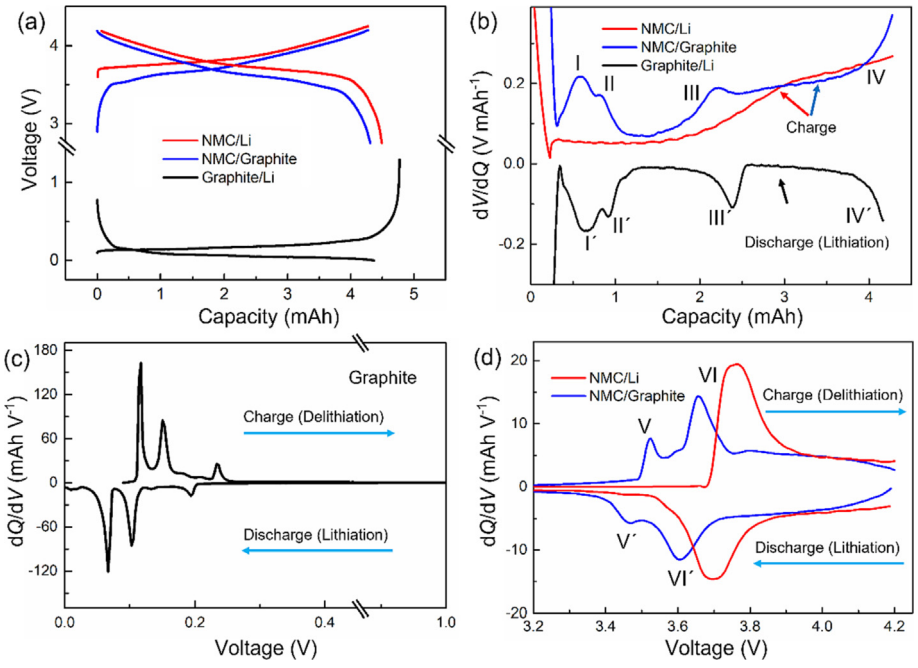

Fig. 2. The electrochemical behavior of electrodes in coin cell. The experiments were performed in coin cells with the combinations of NMC/Li (2.75–4.2 V, 0.1 C), NMC/Graphite (2.75–4.2 V, 0.1 C) and Graphite/Li (0.001–1.5 V, 0.1 C). (a) Charging and discharging curves for the three types of coin cells; (b) the DV curves corresponding to the charging process in a full cell; (c) IC curves of the graphite anode; (d) IC curves of the NMC/Li and NMC/Graphite.

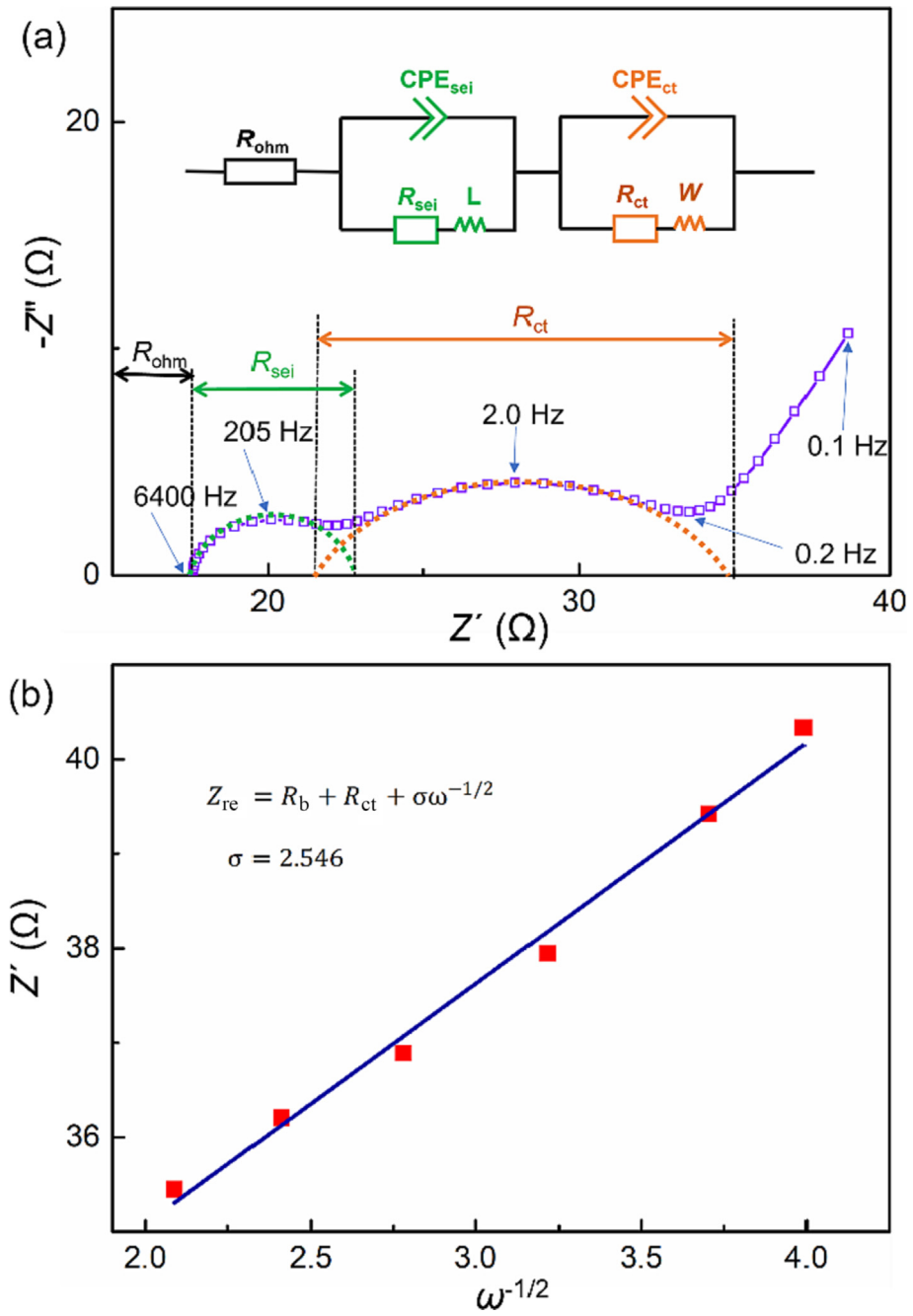

Fig. 3. (a) Typical EIS spectra of the Li-ion cell and the equivalent circuit used to fit the Nyquist curve; (b) the relationship between Z' and $\omega^{-1/2}$ based on (a).

$$Z_{re} = R_{ohm} + R_{ct} + \sigma\omega^{-1/2} \quad (4)$$

$$\omega = 2\pi f \quad (5)$$

where R is the gas constant (8.314 J $mol^{-1}K^{-1}$), T is the absolute temperature (298 K), A is the surface area of the electrode, n is the number of the transferred electrons per molecule, F is the Faraday constant (96,485 C/mol), C is the concentration of Li^+, R_{ohm} is the charge transfer resistance, and ω is the angular frequency.

R, A, n, F, C, and T are the same for the four types of full batteries used in this research. Therefore the relative change in Li-ion diffusion rate (D_{Li}^+ / initial D_{Li}^+) can be calculated, such as D_1:D_2:D_3:D_4=$\frac{1}{\sigma_1^2}:\frac{1}{\sigma_2^2}:\frac{1}{\sigma_3^2}:\frac{1}{\sigma_4^2}$, where the Warburg factor (σ) is the slope of the fitted line, as shown in Fig. 3(b). In this way, the impedances and the trend of the relative change in the Li-ion diffusion rate can be calculated.

3.3. Mechanism identification

The voltage curves of the 18650 full cells in the four aging cases are shown in Fig. 4. All the curves show the plateau and the overall shape very similar to the charging/discharging curves of the NMC/-graphite coin cell, presented in Fig. 2(a). This indicates that it is feasible to study the degradation indicators by the coin cells in Section 3.2. In the charging curves shown in Fig. 4, a lower initial charging voltage corresponds to a higher final charging capacity as well as a higher discharging capacity in every case. Therefore, the increase of the capacity is related to the increase in the electrochemical window of charging in full cells. For this phenomenon,

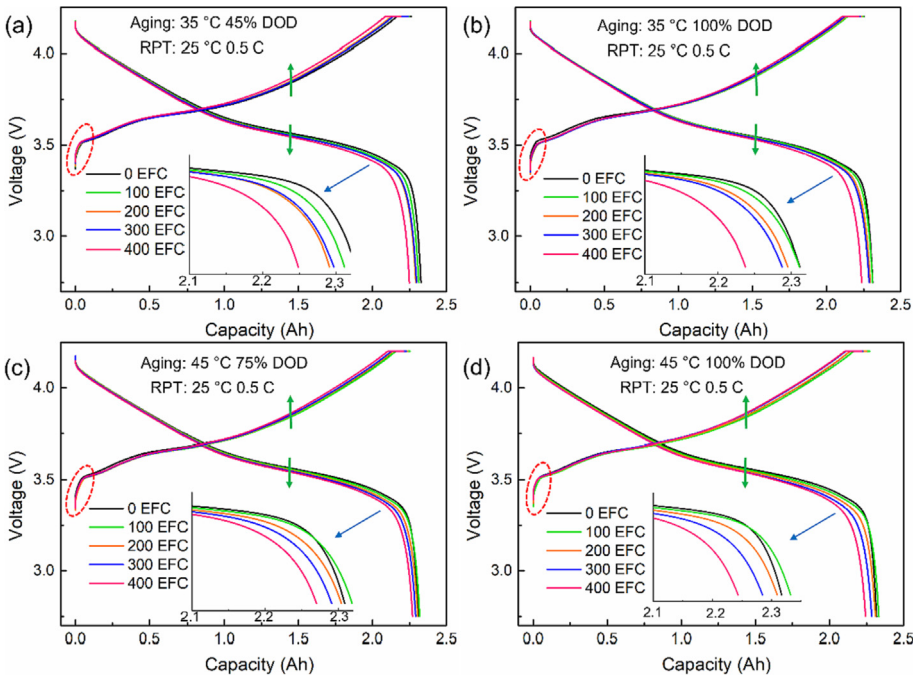

Fig. 4. Charging/discharging curves of the 18650-type cell aging in (a) case 1; (b) case 2; (c) case 3; and (d) case 4.

the most common explanations come from Dubarry's electrochemical modeling, where the simulation results show that the loss of anode graphite will lead to an increase in the main discharging voltage plateau (about 3.7 V), resulting in an increased capacity of the full cell [11]. Obviously, this simulation result cannot be used to explain the capacity increasing behavior in our experiment, because, in all the cases, the main discharging plateau shows a decreasing trend with the cycling evolution, as marked with the green arrow in Fig. 4.

The DVA and ICA techniques were used to study the electrochemical behavior of the 18650 full cells based on the capacity-voltage curves presented in Fig. 4. The IC curves corresponding to the cells aged in the four considered cases are shown in Fig. 5(a–d). The curves exhibit similar characteristic and shape to the NMC/Graphite coin cell in Fig. 2(b and d). This further proves that the mechanism analysis described in Section 3.2 is applicable to full cells.

Based on the indicators discussed in Section 3.1 (i.e., for an IC curve, the main peak intensity represents the amounts of active materials while the secondary peak is related to the available graphite in the anode), the intensity of the main peak around 3.7 V decreases with the number of EFCs for all cases; this behavior is related to the loss of active materials in the positive electrode or negative electrode. Regarding the peak around 3.53 V, it shows a decrease and a displacement towards right trend for cases 1. The decrease of peak intensity means that the graphite contributes less capacity in this phase transition process due to the reduced active graphite. The reason for the shift of the 3.53 V peak towards right is due to the increase in the internal resistance of full cell, corresponding to a reduced electrochemical window as well as a lower capacity. The case 3 only show a decrease trend in main peak of IC curve, and there is no change in secondary peak of IC curve and DV curve, which is consistent with the stable cycling performance in Fig. 1. On the contrary, the peak intensity at 3.53 V in case 3 and case 4 show an increasing trend, which means an increase in the available capacity of the graphite anode. Finally, the shift of the peak towards a lower voltage direction in case 2 and case 4 corresponds to a wider electrochemical window as well as an increased capacity in the full cell. This is consistent with the lower initial charging voltage illustrated in Fig. 4(c and d).

The DV curves, which can clearly show the gap between two adjacent phase transitions, for the four cases are shown in Fig. 5 (e–h). As expected, the main peak in the DV curves shifts to left with the cycle evolution for case 1 because the graphite fails to adequately accommodate the Li-ions. However, the main peak in DV curves of case 3 and case 4 unexpectedly shift to high-capacity direction with the cycling, which means an extended graphite lithiation plateau as well as more available graphite in anode. For further analysis, we have to employ electrochemical impedance spectroscopy (EIS) technique to measure the impedance in battery.

The evolution of the EIS spectra of the full cells during the first 400 EFCs, in each of the four aging cases is presented in Fig. 6; the EIS have been measured at 90% SOC and the curves were fitted using the circuit presented in Fig. 3(a). The evolution during aging of the elements of the circuit is presented in Fig. 6(b).

As shown in Fig. 6(b), there is a minor change in R_{ohm} for case 1. In the more severe aging conditions of case 2, case 3, and case 4, the R_{ohm} increases gradually. The increase of R_{ohm} is more obvious in case 4, as the higher temperature and the larger DOD range accelerate the degradation of electrolyte, separator, and current collector. The R_{sei} shows an increasing trend in all four cases, which is related to the continuous formation, shedding and precipitation of the SEI film, resulting in an increased interface impedance. The mechanism will be discussed in section 4, specifically. The R_{ct} trends to increase for all four cases, which can be attributed to crack formation or structural changes in the graphite and NMC during cycling, resulting in a poor electronic conductivity [13]. However, the R_{ct} shows the same gradually increasing trend, as observed for the capacity, from case 1 to case 4. Furthermore, the Li^+ diffusion rate shows an increasing trend with cycling evolution in cases 2–4 (see Fig. 6b).

In conclusion, there is an increase in capacity of the first 100–300 cycles of the full cell, which is more obvious in a higher temperature and larger DOD aging cases. From the analysis of the *Q-V*, IC, and DV results, it can be concluded that the graphite anodes

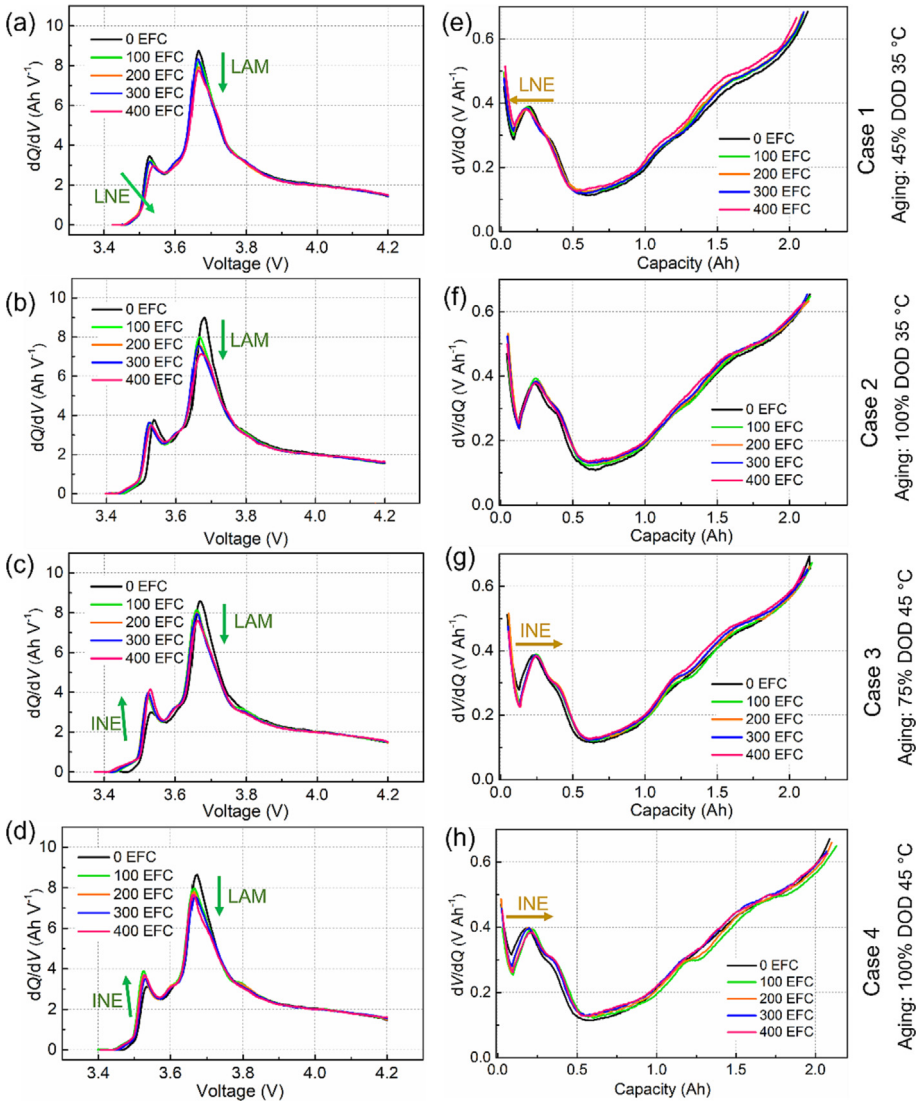

Fig. 5. IC and DV curves for full cell aging at (a, e) case 1; (b, f) case 2; (c, g) case 3, and (d, h) case 4. The curves are derived based on the capacity measurements performed at 25 °C and 0.5 C-rate. LAM represents the loss of active materials, such as positive electrode and negative electrode; LNE represents the loss of available negative electrode; INE represents the increase of available negative electrode in cycling.

cycled at 100% DOD exhibited enhanced graphite anode characteristics with the cycling. Furthermore, EIS further proves that the Li^+ diffusion coefficient in the graphite anode has improved with the cycling in the same conditions. These behaviors correspond well to the increase in the battery capacity, which is observed in the initial cycling stage. However, the charge-transfer resistance increases obviously, especially for cycle aging at elevated temperatures and larger DODs. The specific reasons are further analyzed from the electrodes and material levels.

4. Capacity increase in the graphite anode

Graphite/Li coin cells were assembled, in which the graphite negative electrode is the same as in the 18650 full cells provided by the same commercial company. Two group coin cells were cycled in the voltage ranges 0.001–0.2 and 0.001–1.0 V, which correspond to 45% DOD and 100% DOD in a full cell. The cycling performance is shown in Fig. 7(a). Due to the high potential of pure graphite (2.8 V, Li vs. Li^+), it contributes a high lithiation capacity when discharged to 0.001 V in the first point. In the large DOD (i.e., 0.001–1.0 V), the capacity shows an increase trend in the initial cycling stage. In contrast, the capacity shows a sharp decreasing trend and then increases in stages, when the coin cell is cycled between 0.001–0.2 V. This performance behavior is consistent with the performance of the 18650 cells, regarding the influence of DOD, as well as with the increasing trend of the secondary peak of the IC curves presented in Fig. 5. Furthermore, as reported in [22], the NMC material exhibits a continuously decreasing trend of the capacity in different DODs. Therefore, one can conclude that the initial capacity increase of the 18650 full cells is caused by the graphite negative electrode.

Ex-situ XRD was performed to study the structure change of the graphite in different state of charges. The IC curves corresponding to the graphite lithiation and delithiation process are shown in the left-hand side of Fig. 7(b). In the IC curve, the middle point is the lithium saturation state, and the lithium content gradually decreases to two sides, where the peaks in the lithiation process correspond to the following transitions $LiC_{30} \rightarrow LiC_{18}$, $LiC_{18} \rightarrow LiC_{12}$ and $LiC_{12} \rightarrow LiC_6$. LiC_6 is the full lithiation state of graphite [23]. The change in lithium content is not only reflected in the voltage of graphite, but also in the evolution of the structure. XRD results of graphite with different charging

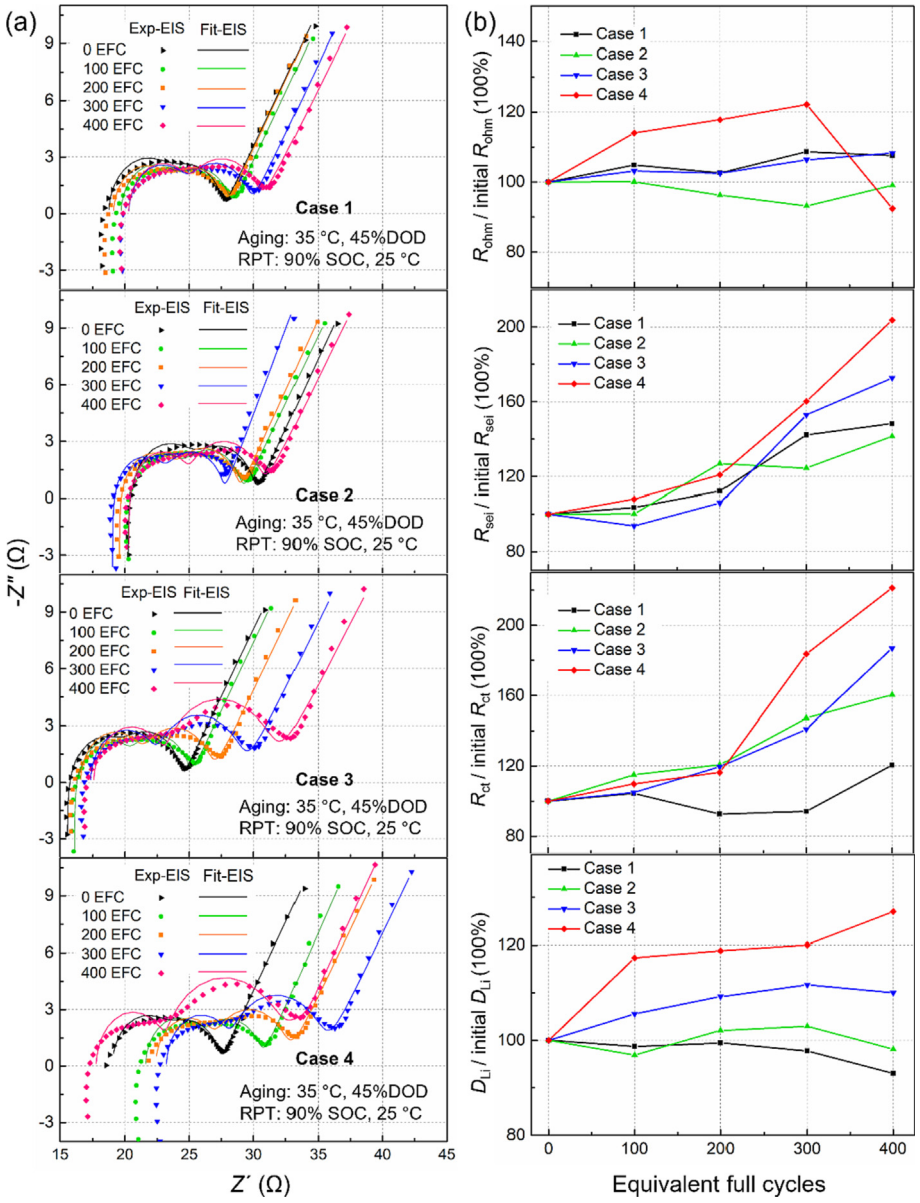

Fig. 6. The experimental and corresponding fitting result of EIS for 18650 cells (a) EIS spectrum of the four cases; (b) corresponds resistances result.

states are shown in the middle of Fig. 7(b). All XRD patterns exhibit evident graphite characteristic peaks at around 27°, which shifts with the voltage evolution. The corresponding *d*-spacing (C–C distance) values are calculated by HighScore Plus software and presented in the right-side of Fig. 7(b). With the voltage decreasing, the C–C distance show an increasing trend due to the increased lithium content. Cycling in a larger voltage range (i.e., 0.001–1.0 V) means a larger variation in the interlayer spacing. When the graphite lithiation occur from 0.27 to 0.001 V, the *d*-spacing (C–C distance) increases by 8.8%, then it gradually recovers. As the variation in *d*-spacing, the SEI film may break down, form again, and lithium salt precipitation, resulting in an increased R_{sei} as also illustrated in Fig. 6.

After 25 EFCs (where 1EFC = 4 mAh), the two-coin cells were charged to a fully de-lithiation state (i.e., 1.5 V), then they were disassembled to perform post-mortem analysis. The XRD patterns of the cycled graphite anodes are shown in Fig. 7(c). For fresh graphite, we have measured a 3.31 Å *d*-spacing. After cycling, the *d*-spacing has increased to 3.47 and 3.66 Å, when aging the cells between 0.001–0.2 and 0.001–1.0 V, respectively. As it can be observed, a larger voltage interval enlarges the graphite interlayer spacing, which is beneficial to the diffusion of Li^+ [24]. This behavior was further proved by EIS results, which are presented in Fig. S2. This is consistent with the increase in Li-ion diffusion coefficient (see Fig. 6), obtained from the EIS analysis, for the full cell aged at larger DOD.

The morphology of the cycled graphite electrodes between 0.001–0.2 and 0.001–1.0 V cases were characterized by FESEM and the images are shown in Fig. 8. For the coin cell cycled between 0.001 and 0.2 V, the FESEM images of cross-section and the EDS of carbon (C) and oxygen (O) elements are shown in Fig. 8, initial RPT tests revealed an abnormal. The graphite particles, with a size of 10–20 μm, are uniformly distributed over the copper current collector. The oxygen element is mainly from the surface of the SEI film and inorganic salt compounds. This indicates that the SEI film is distributed on the surface of the cycled electrode. As shown in Fig. 8, initial RPT tests revealed an abnormal, the intact graphite particles exhibit smooth surfaces and bond well with the copper

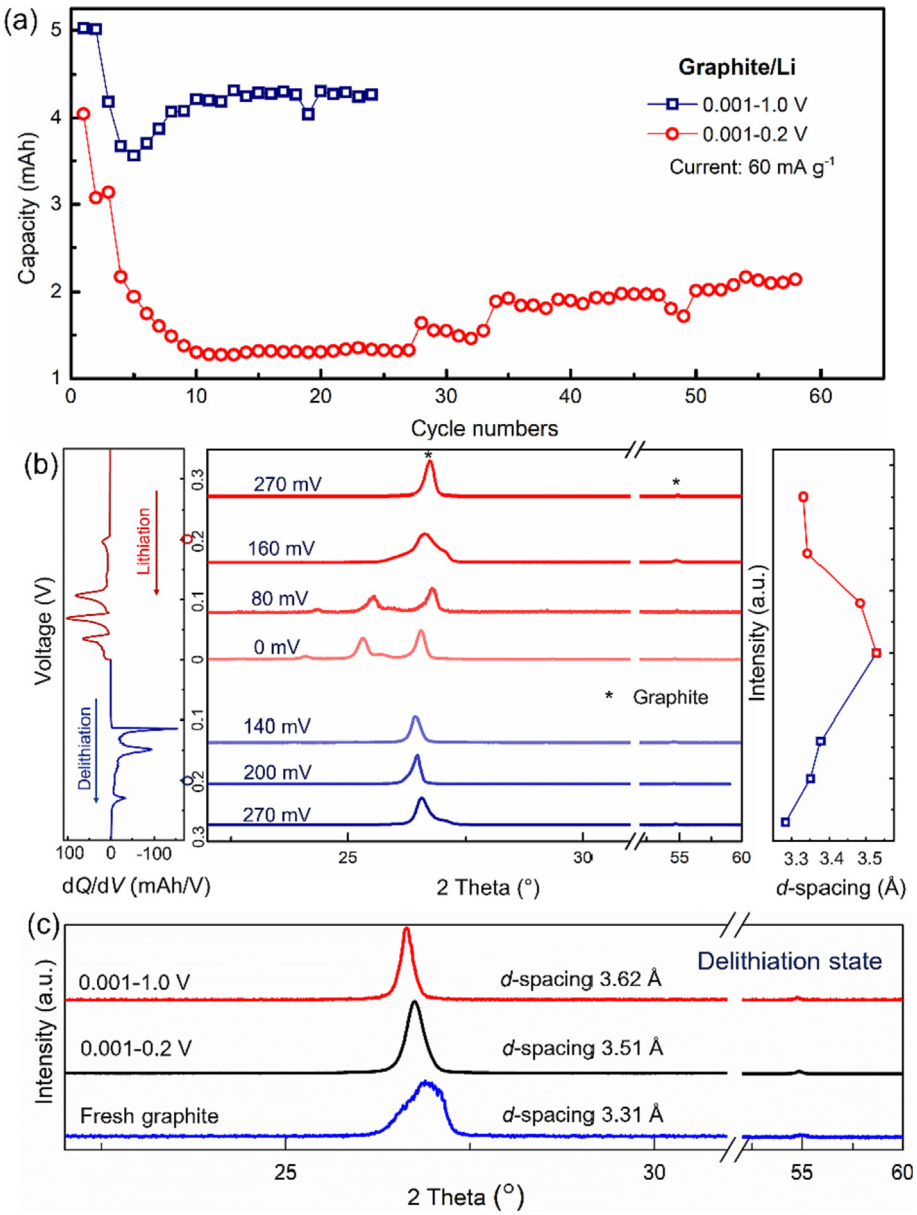

Fig. 7. (a) The cycling performance of graphite anode in the voltage range of 0.001–1.0 and 0.001–0.2 V. Ex-situ XRD patterns for (b) the structure evolution during electrochemical de-/intercalation of Li-ions half cells, and the corresponding d-spacing in graphite layer calculated by Highscore software; (c) graphite anode after 25 equal full cycles in different voltage ranges in a 1.5 V state of voltage.

current collector. As reported in [25], this smooth surface is named basal plane; it is difficult for Li^+ to pass through this basal plane because the internal carbon atoms form tight covalent bonds with their neighbors making them very chemically resistant, thus, resulting in a low Li^+ diffusion coefficient. The slow diffusion rate leads to the accumulation of Li^+ in the anode-electrolyte interface, forming "dead lithium" and lithium dendrites [26]. As shown in Fig. 8(c), the negative electrode surface grows lithium dendrites with a small size of several nanometers as well as the SEI film. The formation of lithium dendrites and of the SEI film is the main cause of loss of lithium inventory and it also damages the graphite, resulting in a capacity decrease. All these explain why the full cells aged with a 45% DOD shows an evident capacity decrease in the initial cycles.

For the coin cell cycled between 0.001 and 1.0 V, the FESEM image of the cross-section is displayed in Fig. 8(d). A soft texture caused by layer separation inside the graphite particles is observed. On the graphite surface, the basal panel disappeared, forming clusters of graphite nanosheets. The increase of graphite spacing will undoubtedly reduce the electronic conductivity, resulting in an increased charge transfer resistance R_{ct} as also reported in Fig. 5. This may be attributed to the larger variation in the graphite interlayer spacing during larger DOD charge and discharge. Thereby, the graphite layer is exfoliated into a nanosheet shape, as shown in Fig. 8(e), which exposes more graphite surface to the electrolyte, resulting in facilitating the Li^+ transport. Consequently, graphite nanosheets accelerate the lithiation and de-lithiation process, and the Li^+ insert in graphite with a lower ionic resistance, causing a lower initial charge

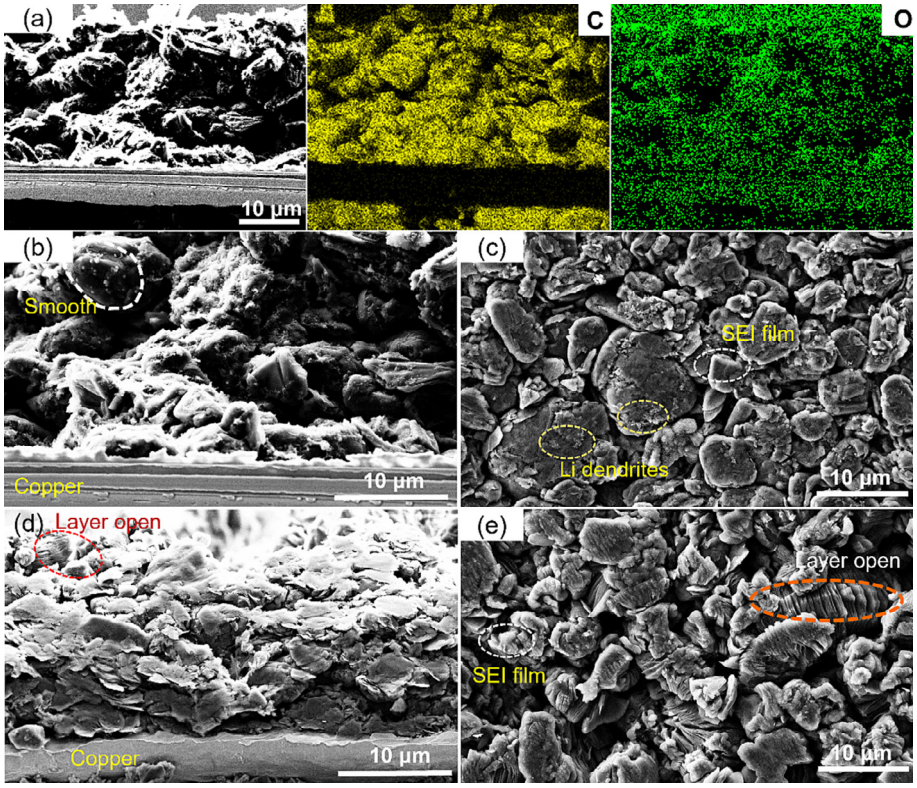

Fig. 8. FESEM images of cycled negative electrodes showing cross-section and surface morphology. (a) Cross section of a negative electrode after cycling the voltage range of 0.001–0.2 V range with EDS distribution maps for carbon and oxygen; (b and c) zoom-in of the cross section and electrode surface for 0.001–0.2 V case; (d and e) zoom-in of the cross section and electrode surface for 0.001–1.0 V case.

voltage (as shown in Fig. 4) as well as an increased capacity of the battery. This explains well why the capacity increases in the initial cycling stage.

5. Conclusions

In this study, the mechanism of the capacity increase, observed in the early cycling stage, of commercial NMC/graphite Li-ion batteries was investigated by non-destructive techniques and post-mortem analysis. The electrochemical behavior related to the capacity increase was studied on the full cell, electrode, and material levels. The results show an increased capacity in the early aging stage, especially for larger DODs (such as 100% DOD and 75% DOD). Temperature exacerbates this process in the case of 100% DOD cycling, and an 1% initial capacity increase was observed in one of the cases. IC and DV curves revealed that more Li^+ can be inserted into graphite with the cycling evolution in cases 2–4. Furthermore, the EIS results show that the Li^+ diffusion rate increases with the EFCs, in case 3 and case 4.

The graphite negative electrode was studied using coin cells, and the *d*-spacing of graphite increased about 8.8% from pure graphite to the full lithiation state. Furthermore, the evolution of *d*-spacing in graphite under cycling shows that it is not recovered completely when graphite is in the delithiated state. The enlarged *d*-spacing reduces the insertion resistance of Li^+, resulting in an increased Li^+ diffusion rate. In terms of morphology, the graphite in cycle-aged cells with large DODs tends to exfoliate into a nanosheet shape, which exposes more surface to the electrolyte. Then, the amount of Li-intercalable graphite has increased and the electrochemical window was enlarged by the potential reduction of the graphite side, resulting in an increased capacity of the battery.

Declaration of competing interest

The authors declare that they have no known competing financial interests or personal relationships that could have appeared to influence the work reported in this paper.

Acknowledgments

Jia Guo and Yaqi Li are supported by a grant from the China Scholarship Council (202006370035 and 202006220024). Jinhao Meng is supported by the National Natural Science Foundation of China (52107229). We like to thank Deyong Wang and Peter Kjær Kristensen for their help in performing the FESEM test, Donghong Yu for his help performing the XRD test, and Kim Houtved Jensen for helping with the experiment platform. Furthermore, we would also like to thank Haidi Energy Technology Co. for providing electrodes, which were used to manufacture the coin cells.

Appendix A. Supplementary data

Supplementary data to this article can be found online at https://doi.org/10.1016/j.jechem.2022.07.005.

References

[1] X. Sui, S. He, S.B. Vilsen, J. Meng, R. Teodorescu, D.I. Stroe, Appl. Energy 300 (2021) 117346.
[2] F.H. Gandoman, J. Jaguemont, S. Goutam, R. Gopalakrishnan, Y. Firouz, T. Kalogiannis, N. Omar, J. Van Mierlo, Appl. Energy 251 (2019) 113343.
[3] N. Yan, H. Zhao, X. Pan, G. Ma, S. Ma, IEEE Trans. Appl. Supercond. 31 (2021) 1–4.

[4] M.-F. Ng, J. Zhao, Q. Yan, G.J. Conduit, Z.W. Seh, Nat. Mach. Intell. 2 (2020) 161–170.
[5] K.A. Severson, P.M. Attia, N. Jin, N. Perkins, B. Jiang, Z. Yang, M.H. Chen, M. Aykol, P.K. Herring, D. Fraggedakis, M.Z. Bazant, S.J. Harris, W.C. Chueh, R.D. Braatz, Nat. Energy 4 (2019) 383–391.
[6] G. Ma, Y. Zhang, C. Cheng, B. Zhou, P. Hu, Y. Yuan, Appl. Energy 253 (2019) 113626.
[7] Y. Zhang, Q. Tang, Y. Zhang, J. Wang, U. Stimming, A.A. Lee, Nat. Commun. 11 (2020) 6–11.
[8] X. Tang, C. Zou, K. Yao, J. Lu, Y. Xia, F. Gao, Appl. Energy 254 (2019) 113591.
[9] B. Gyenes, D.A. Stevens, V.L. Chevrier, J.R. Dahn, J. Electrochem. Soc. 162 (2015) A278–A283.
[10] M. Lewerenz, J. Münnix, J. Schmalstieg, S. Käbitz, M. Knips, D.U. Sauer, J. Power Sources 345 (2017) 254–263.
[11] M. Dubarry, C. Truchot, B.Y. Liaw, J. Power Sources 219 (2012) 204–216.
[12] Y. Kobayashi, H. Miyashiro, A. Yamazaki, Y. Mita, J. Power Sources 449 (2020) 227502.
[13] C. Pastor-Fernández, K. Uddin, G.H. Chouchelamane, W.D. Widanage, J. Marco, J. Power Sources 360 (2017) 301–318.
[14] B. Ospina Agudelo, W. Zamboni, E. Monmasson, Energy 234 (2021) 121224.
[15] W. Pan, X. Luo, M. Zhu, J. Ye, L. Gong, H. Qu, J. Energy Storage 42 (2021) 103072.
[16] H. Kato, Y. Kobayashi, H. Miyashiro, J. Power Sources 398 (2018) 49–54.
[17] W. Li, D. Cao, D. Jöst, F. Ringbeck, M. Kuipers, F. Frie, D.U. Sauer, Appl. Energy 269 (2020) 115104.
[18] Y.B. He, F. Ning, Q.H. Yang, Q.S. Song, B. Li, F. Su, H. Du, Z.Y. Tang, F. Kang, J. Power Sources 196 (2011) 10322–10327.
[19] M. Gaberšček, Nat. Commun. 12 (2021) 19–22.
[20] Y. Wang, J. Zhang, J. Xue, X. Ke, G. Liang, Ionics 27 (2021) 4687–4694.
[21] Y. Chen, Y. Li, W. Li, G. Cao, S. Tang, Q. Su, S. Deng, J. Guo, Electrochim. Acta 281 (2018) 48–59.
[22] K.J. Park, J.Y. Hwang, H.H. Ryu, F. Maglia, S.J. Kim, P. Lamp, C.S. Yoon, Y.K. Sun, ACS Energy Lett. 4 (2019) 1394–1400.
[23] A. Missyul, I. Bolshakov, R. Shpanchenko, Powder Diffr. 32 (2017) S56–S62.
[24] Y. Tang, X. Wang, J. Chen, X. Wang, D. Wang, Z. Mao, Carbon 174 (2021) 98–109.
[25] H.L. Andersen, L. Djuandhi, U. Mittal, N. Sharma, Adv. Energy Mater. 11 (2021) 1–21.
[26] Y. Chen, X. Dou, K. Wang, Y. Han, Adv. Energy Mater. 9 (2019) 1–7.